Appendix A: Beam Dynamics

In Chapter 2 we outlined a development of the dynamics of a particle beam from the single-particle trajectory equation without space charge forces, progressing through the envelope equations and the Courant-Snyder [26] invariant without space-charge forces. Space-charge was included first in a linear field model using the distribution of Kapchinskij and Vladimirskij [30], or the "K-V" distribution. In essence, the K-V distribution allows the same handling of particle trajectories as the zero-current case because the space-charge field behaves as a distributed linear lens. The particle beam envelope is then calculated self-consistently with its own space-charge field. This is a numerical exercise involving the fitting of the envelope initial conditions to provide a periodic envelope.

We then remarked on the more general approach to the problem given by Sacherer [31] and Lapostolle [14]. By averaging the trajectory equation over the phase space distribution function of a beam, they obtained equations for the RMS radii of the beam in the two transverse planes. These equations are identical in form to the K-V envelope equations, at least for a beam with a real space distribution having elliptical symmetry. We now continue with some aspects of space-charge dominated transport in particular.

A.1 Space-Charge Dominated Transport

Even in the limit of zero emittance, the lattice will transport only a certain limiting current for a given σ_0 and bore radius. In the smooth approximation, this current depends on σ_0 for a constant bore radius, R_Q, as

$$I_{\text{S.A.}} = \frac{\pi \epsilon_0 m v_z^3}{2q} \left(\frac{R_Q}{L} \right)^2 \sigma_0^2, \qquad (A.1)$$

where we have written the equations in terms of a "period," $2L$, over which the phase advance in the absence of current is given by σ_0. In this formula, σ_0 is in units of radians.

For an A.G. lattice, the current does not have this parabolic rise with σ_0 because of the envelope flutter required for the strong focusing. For a beam of zero emittance, the space charge forces cancel the external focusing and the beta function diverges. We have calculated the maximum beam radius for a beam with zero emittance in a thin lens FODO (see section 2.2.1) channel, using the envelope equations, Eqns. 2.5. With lenses of focal length $\pm f$ and separation L, we solved the envelope equations in the approximation that the sum of the beam radii is nearly constant to obtain

$$R_{\max} = \sqrt{\frac{qI}{2\pi\epsilon_0 m v_z^3}} \frac{L}{2} \frac{2 + \sin(\sigma_0/2)}{\sin(\sigma_0/2)},$$

where $\sin(\sigma_0/2) = L/2f$. We now obtain

$$I_{\text{A.G.}} = \frac{\pi\epsilon_0 m v_z^3}{2q} \left(\frac{R_Q}{L}\right)^2 \left(\frac{2\sin(\sigma_0/2)}{1 + \frac{1}{2}\sin(\sigma_0/2)}\right)^2. \qquad (A.2)$$

This equation is written so that the leading factors are of the same form as for Eqn. A.1. The dependence on σ_0 of Eqn. A.2 reduces to that of Eqn. A.1 in the limit of low σ_0.

In the absence of instabilities, the ideal beam current in this approximation would appear to peak at $\sigma_0 = 180°$, with a value of 2.8 times the $\sigma_0 = 60°$ value. The parameterization in terms of the sine function hides the fact that $L/2f$ can exceed unity. The above result is valid within the range of $L/2f \leq 2$, rather than the zero-current limitation of $L/2f \leq 1$, but the same single-particle resonance with the focusing would require $\sigma_0 < 180°$ even in the absence of collective instability of the beam. This is in marked contrast

to the acceptance as a function of lattice strength for emittance-dominated beams. The limitations of alignment would require that this limit not be approached very closely, even in the absence of collective instability. However, even at $\sigma_0 = 80°$, the current is 1.5 times that for the same lattice at $\sigma_0 = 60°$. In a regime not limited by attainable focusing field gradients, much could be gained by increasing σ_0 to somewhat above 60°. This provides good reason for attempting the strongest focusing possible, and carefully probing the instablility limits of high-current beam transport.

A.2 Useful Approximate Calculations

In the process of this work, we found it simple and accurate to model the lenses as hard-edge quadrupoles, accounting for the space-charge forces in a smooth approximation correction to the focusing of the individual quadrupoles. We fit the occupancy factor of the quadrupoles, η, where

$$\eta \equiv \frac{L_Q}{L},$$

L_Q is the actual length of the lenses,and $2L$ is the period of the focusing, to the single-particle phase advance calculated numerically as a function of voltage. We found that $\eta = 0.593$ gave very good agreement with the model σ_0 as a function of V_Q from the ideal lattice calculation without space-charge, as shown in Table A.1.

Rather than solving the envelope equations numerically each time we needed an estimate for the matched beam size or for σ for a particular set of beam parameters, we found that we could replace the space-charge forces in a simple way and replace the envelope equation integration by a transfer matrix calculation. In place of the space-charge forces, we calculated the

σ_0 (EE)	σ_0 (SSC)	ϵ_{unn}/Q	R_{max} (EE)	R_{max} (SSC)	σ (EE)	σ (SSC)
59°	59°	0.0185	19.0	20.1	8°	7°
78°	78°	0.0177	15.9	16.7	12°	11°
83°	83°	0.0215	15.5	16.3	17°	15°
88°	88°	0.0286	14.8	15.5	24°	21°
91°	91°	0.0242	13.7	14.5	22°	19°
94°	94°	0.0324	12.5	13.0	29°	26°
97°	97°	0.0800	13.1	13.6	57°	52°
102°	102°	0.100	11.1	11.3	67°	63°
116°	116°	0.172	8.9	9.0	93°	88°
124°	124°	0.151	13.3	13.1	99°	92°
135°	134°	0.156	9.8	9.6	108°	101°
144°	142°	0.145	11.6	11.3	114°	104°

Table A.1: Smooth space charge model compared with envelope equation integration. We have included the relative values of the emittance and current through the quantities appearing in the envelope equation, as the ratio of the unnormalized emittance, ϵ_{unn}, to the generalized perveance, Q. Units for the various quantities are °/period for the tunes, π meter radian for ϵ_{unn}/Q, and mm for radius. The notation (EE) represents quantities calculated using the envelope equations, while (SSC) denotes the same physical quantities estimated by averaging the space-charge forces along the lattice.

equivalent defocusing lens strength for the beam, K_B, as

$$K_B = \frac{Q}{2R_0^2} = \frac{qI}{\pi\epsilon_0 m v_z^3 R_0^2},$$

taking the radius R_0 between quadrupoles as the appropriate size for the beam to calculate the average space-charge defocusing field. We calculated the quadrupole strength, K_Q, as

$$K_Q = \frac{4qV_Q}{m v_z^2 R_Q^2},$$

and used net focusing and defocusing strengths of K_+ and K_-, respectively, of

$$K_+ = K_Q - K_B$$

$$K_- = K_Q + K_B.$$

The drift portion of the lattice is then treated as a defocusing lens.

After calculating the transfer matrix through one period, beginning at the midplane between quadrupoles and with a particular K_B, we used the relationship $R_0^2 = \beta\epsilon$ to calculate the ratio ϵ/I. The half-trace of the transfer matrix including space-charge forces gives the corresponding σ. We found very good agreement between this model and the envelope integration model using the K-V equations. The thin lens lattice is solvable in simple closed form for $\epsilon = 0$, with the result for the transportable current given above in Eqn. A.2. The result for the maximum current through a given bore in the $\epsilon \to 0$ limit for the smooth space-charge model is

$$I_{\text{s.s.c.}} = \frac{\pi\epsilon_0 m v_z^3}{2q} \left(\frac{R_Q}{L}\right)^2 \left[\frac{2\sin(\sigma_0/2)}{\exp\left[\frac{1}{2}\sin(\sigma_0/2)\right]}\right]^2 \qquad (A.3)$$

as a function of σ_0, where we have written the equation in the same form as Eqns. A.1 and A.2. For small values of $\sin(\sigma_0/2)$, Eqn. A.3 reduces to the envelope equation result. Even at extreme lattice strengths this model agrees well with results obtained from the envelope equations. Even for σ_0 as high as 180°, the ratio of limiting currents from the approximate solution of the envelope equations above and this smooth space charge calculation is

$$\frac{I_{\text{s.s.c.}}}{I_{\text{A.G.}}}\bigg|_{180°} \simeq 0.83,$$

and for $\sigma_0 = 90°$

$$\frac{I_{\text{s.s.c.}}}{I_{\text{A.G.}}}\bigg|_{90°} \simeq 0.90.$$

The ratio of the currents is about 0.95 for a 60° lattice. These two approximations to the solution of the envelope equations converge to the exact solution in the limit of small lattice strength. Because the current is proportional to the product of the two beam dimensions, the actual beam radius is less in error than the above numbers for relative current would suggest. The S.S.C. form is only a few percent in error for calculating maximum envelope radius (and σ) as a function of ϵ, I, and σ_0 over a very wide range of lattice strength, particularly if the current is a significant factor in the transport. We implemented this procedure on a programmable hand calculator for quick estimates of σ, R_+, and R_0 for the SBTE, as well as for stability estimates for Cs^{+2} ions in the space charge field of the Cs^+ beam.

Appendix B: Faraday Cups

The charge collecting diagnostics must measure the total ion beam current with minimal error. In addition, emittance measurements require the precise relative measurement of currents down into the sub-microampere range. For this purpose, a large secondary emission gain would be very useful if the gain were uniform. In this appendix we discuss the methods we used to attain these goals and the uncertainties of the measurements. We chose to measure the total beam current by direct ion collection, and to use the emittance diagnostic cups in the secondary emission (SE) mode.

B.1 Secondary Electron Yields

Relative measurement of small beam currents by diagnostics using secondary particle emission as an amplifying mechanism is very easy. Homogeneous plate materials are not expected to show large variation in secondary electron emission gain over their surfaces. In our measurements, we have seen only variations due to bias fields and angle of primary particle impact. The measured secondary electron yield on stainless steel sheet stock for normally incident Cs^+ ions in the 120–160 keV range is 12, depending only weakly on applied bias field up to a few kV/cm strength. This is the result both for the full beam and for very highly attenuated beams during emittance scans. The average gain across the diameter of 0.020 in tungsten wires has been measured to be about the same for our multiwire profile monitors, again about a factor of 12.

B.2 Slit Cups

The slit cups (shown in Fig. 3.12) are used only for measuring the emittance or current profile of a beam. This function is served very well by the reverse biased secondary emission mode. The cup bias response in this mode

is flat from 100 to 500 V. We used ± 300 V biases for $G2$ and C, respectively. In the slit cups, the "grid" $G1$ is the slit itself and is expicitly grounded. The ratio of back- to forward-biased current signals is about 10, a somewhat lower ratio than found for the other cups, but we do not consider the difference significant.

B.3   Absolute Current Measurement

### B.3.1   Shallow Faraday Cups

When we attempt to make absolute current measurements with a shallow Faraday cup, we must introduce at least one grid to suppress secondary emission from the collector. We use two grids, each of at most 98% transparency. We thus expect to have electron currents of as much as 40% of the incoming beam current flowing near the grids and must control the electrons very well in order to measure the ion current accurately.

We have labeled the electrodes as in Fig. 3.9. When grounding $G1$ and biasing $G2$ negative and C positive, the cup current did not crisply saturate. The cup current continued to drop very slowly as the potential difference $C - G2$ was raised. We found a somewhat crisper saturation for the reverse bias, secondary emission mode, but the current continued to rise very slowly as the potential difference $C - G2$ was lowered.

Secondary electrons from the positively biases collector are energetically unable to escape to grounded surfaces, and the negative $G2$ bias prevents the e^- from being drawn out by the beam potential of about $+600$ volts. Some e^- from $G2$ may be collected at C. With the grid $G1$ still at ground potential we found a transient negative current signal at the tail of the beam pulse. The time development may be seen in Fig. B.1. These effects are shown in Fig. B.1. The negative transient signal as a function of pulse duration is quite well correlated with the deviation of the current pulse shape from a square
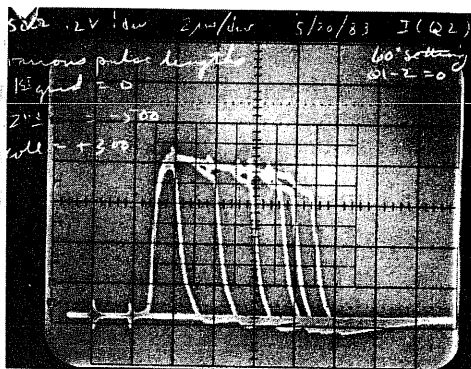
(a)
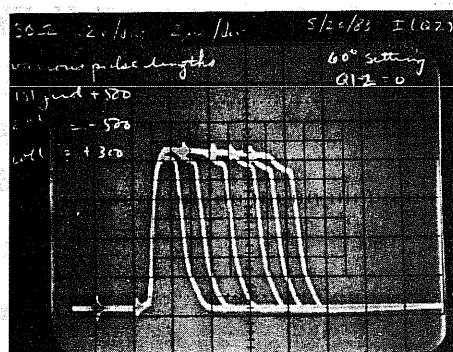
(b)
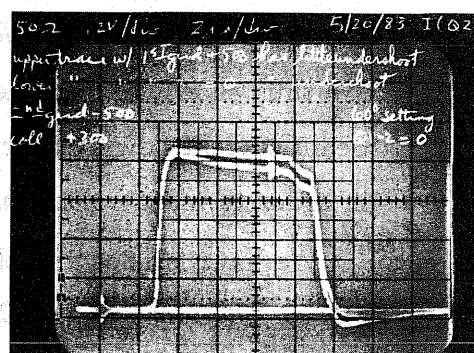
(c)

XBB 864-2706

Figure B.1: Current response of the SFC. With the first grid grounded, the head and tail of the current pulse showed a saturation in SFC response at different biases (not shown). After we had chosen a bias configuration which gave a reasonable saturation over the length of the pulse, we noted an undershoot of the measured current at the end of the pulse. By overlaying pulses of various length (a), we found that the envelope of the undershoot closely approximated the deviation of the SFC response from the flat current vs. time we had expected. While keeping the same positive bias on the collector, we found that we could suppress the undershoot by biasing the first grid, $G1$, to a higher positive potential than we biased the collector (b). A positive bias on $G1$ had little effect for values lower than the collector potential, but with the biases $G1 = +500$ and $G2 = -500$, the current showed no variation over approximately the range $100 < C < 400$, and the undershoot was almost totally eliminated. We hopted to use $G1 = +500$, $G2 = -500$, and $C = +300$. The comparison between the initial and final bial configurations is shown in (c).

pulse. However, with bias fields of the order of a 1 kV/cm, the ~ 1 μsec decay time scale of the undershoot indicates that it is an ion effect rather than an electron effect. We must assume that there is a small secondary yield of positive ions, which are flowing from the collector to the grids.

We found that biasing $G1$ to $+500$ V essentially eliminated the cup undershoot. Any secondary positive ions will be unable to penetrate the $G1$ bias and will be reflected preferentially to the collector. An additional benefit is the enhancement of the local electric field at $G2$ on the upstream side, minimizing entry of secondary electrons into the $G2$–C region. We thus chose to operate the SFC's with a collector bias of $+300$ volts, biasing the grids G1 and G2, respectively, to ± 500 volts.

The shallow cups were fabricated at various times, with grids of differing transparency, and so had different calibration factors. The comparison can be seen in Fig. 5.3, showing the direct response of all the cups to a beam with no known Cs^+ component loss exceeding about 2% over the lattice length.

B.3.2 Deep Faraday Cups

The DFC (deep Faraday cup) was designed by Dr. C. Kim using Hermannsfeldt's EGUN [34] program to calculate the axial potentials, including the beam space-charge. The resulting design is shown in Fig. 3.10. The collector and repeller biases may be raised to ± 5 kV. Operation with $C = +2\text{kV}$ and $R = -2$ kV will result in a potential minimum along the axis of -200 volts even in the presence of 15 mA of 120 keV Cs^+. This provision was made because "electrons are everywhere," and we wanted to avoid any trouble with primary electrons.

The DFC bias curve saturates crisply at both polarities, the bias ring preventing electrons from entering (negative bias) or leaving (positive bias) in each case, as shown in Fig. B.2. The ratio of the currents in the two bias

Deep Faraday cup bias curves
for various bias conditions
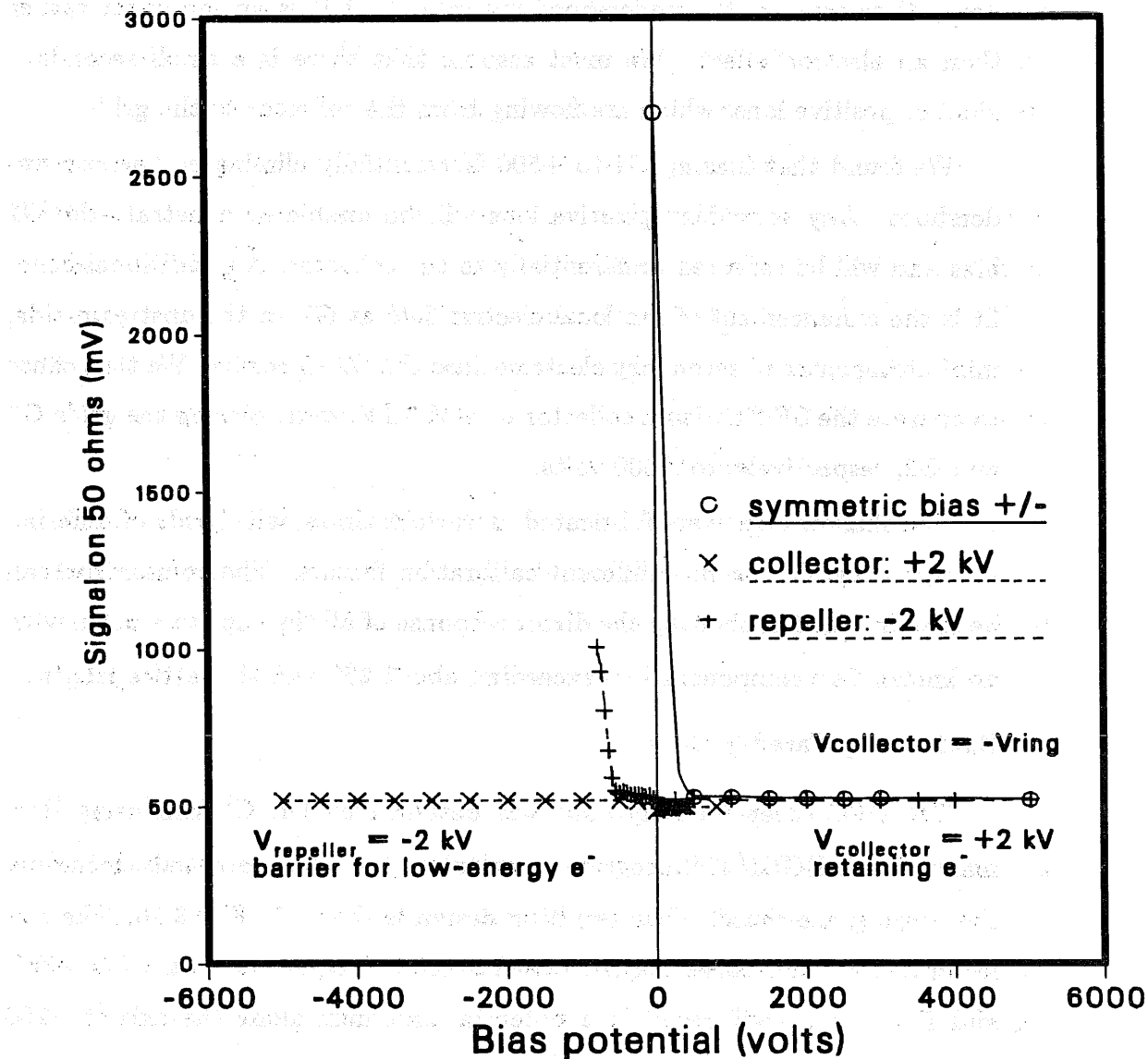
XBL 865-1839

Figure B.2: Bias curves for the DFC. With biases for the collector and the repeller ring differing only in polarity, the DFC response saturated cleanly in both the secondary electron retention and secondary emission modes. The ion current saturated at ±500 V, respectively, for the collector and repeller, but we operated at the design bias of ±2 kV. This maintains a negative potential across the central plane of the repeller ring to prevent any possibile entry of low-energy electrons.

modes is again about 12. The absolute current calibration is thus subject to error primarily by secondary positive ion emission. The bore clearance is sufficient to avoid all problems of primary ion impact on the repeller ring. The major compromise lies in the inherently poor spatial resolution that arises from the capacitive coupling of the cup to the beam it is measuring. The slow beam results in a risetime for current perturbations of only 150–200 ns because the coupling of a given beam ion to the cup takes place over a 2–3 in distance centered at the 1 in gap separating the collector and repeller.

B.3.3 Secondary Ion Effects

We estimated the magnitude of the error in current measurement caused by the secondary ions by using the DFC near the source, where the current pulse drops sharply at the pulse end. Typical data are visible in Fig. 5.3. The undershoot we saw in the SFC traces is visible for short fall-times of the current pulse. The DFC after Q82 showed no undershoot because the long pulse tail masked any negative current transient. The magnitude of the ion error signal is about 4% of the total current. Some of the ions are probably collected by the repeller ring, but with too low an energy to result in significant secondary electron emission. Because we do not believe that the true beam current is less than the indicated value, and because the secondary ion emission (assumed to be the dominant error mechanism, lowering the measured current below the true value) appears to affect the current reading by no more than about 4%, we quote our uncertainty in the value of the beam current as $I = I_{\text{measured}}{}_{-0\%}^{+4\%}$.

Appendix C: Emittance Increase due to Grids in the Beam Path

In the SBTE, we use grids at the source for two purposes. The primary purpose is to terminate the accelerating field without grossly defocusing the beam. We also use additional, externally biased grids to increase the beam emittance in a controlled fashion. We will discuss the performance and mechanism of operation in this appendix.

Fine-grained spatial variation of a transverse electric field at the grid scatters the beam particles out of their former phase space positions. We will use $4\epsilon_{RMS}$ to parameterize the beam emittance, given by

$$4\epsilon_{x \text{ RMS}} = 4\langle(x - \overline{x})^2\rangle^{\frac{1}{2}}\langle(x' - \overline{x'})^2\rangle^{\frac{1}{2}} = 2\tilde{x} \times 2\tilde{\theta}_x. \qquad (C.1)$$

We use the quantity $2\tilde{x}$ for the beam radius, and it is convenient to use $2\tilde{\theta}$ as the angular spread parameter.

In the SBTE, the beam particle energy is an order of magnitude larger than the potential applied to the grids, and the impulse approximation is sufficient to calculate the velocity space perturbation of the beam. The intrinsic RMS angular spread of the beam adds in quadrature to the RMS grid perturbation angle, so that the grid perturbation adds a term in quadrature to the intrinsic source emittance.

Because the measurements reported in this Appendix were not the central concern of the program, and were compiled from scattered results throughout the time span of the experiment, some of the data are from operation with the original, 160 keV injector configuration, and some are from the later configuration operated with a particle energy of 120 keV. As a result, some conceptually related calculations are reported for different particle energies.

C.1 Mechanism

The two sources of electric field acting upon the grid are the beam self-field and externally applied fields. We will first examine the effect of a single grid terminating the acceleration field of the injector, and then of an externally biased grid array.

We will model a parallel-wire grid as an array of slots, each as in Fig. C.1. In the impulse approximation, a particle transiting the slit experiences a lens action with an equivalent focal length

$$f_{\mathrm{s}} = \frac{2T}{\Delta E_{\parallel}} \tag{C.2}$$

where T is the particle kinetic energy in eV and $\Delta E_{\parallel}$ is the change in longitudinal field.

As shorthand, we define a parameter α by

$$\alpha \equiv \frac{\Delta E_{\parallel}}{4T}. \tag{C.3}$$

For a parallel-wire grid, calculating the perturbation in the plane transverse to the grid, we have
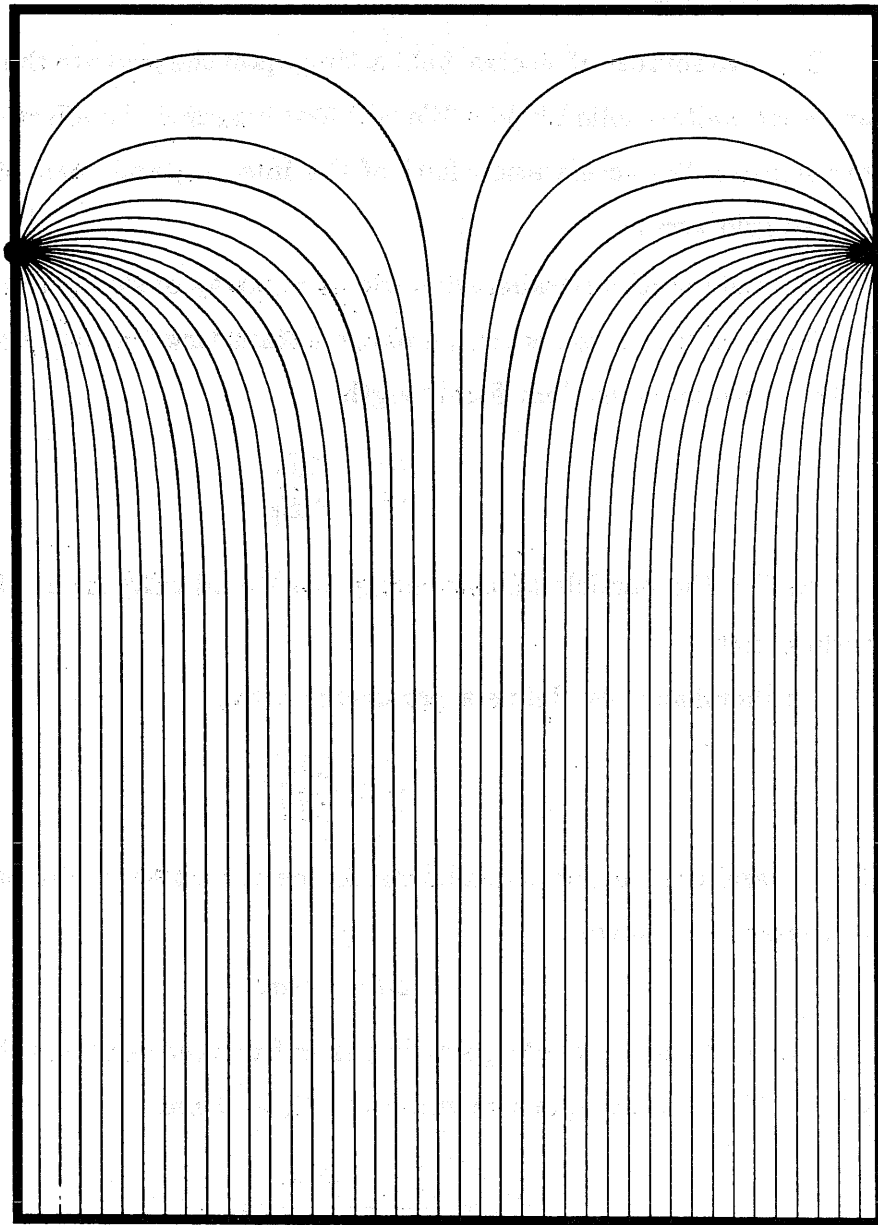
$$\Delta \theta_t = 2\alpha r,$$

where r is the distance the particle passes from the center of the gap between wires. Thus, for an aperture width of $2R$, we have

$$\langle \theta_t^2 \rangle = \frac{\int_0^R (2\alpha r)^2 \, dr}{\int_0^R dr} = \frac{4}{3}(\alpha R)^2$$

in the plane perpendicular to the slit. When the grid is oriented at 45° with respect to the x and y planes, the result is

$$2\tilde{\theta}_x = 2\sqrt{\frac{2}{3}}\, \alpha R \simeq 1.63 \alpha R \tag{C.4}$$

XBL 865-1759

Figure C.1: We show field lines in one cell of a parallel-wire grid, with wires at either side of the figure, perpendicular to the plane of the page. The boundary conditions include a uniform field in the vertical direction at the bottom of the figure, with a field-free region far above the grid. The electric field focuses the particles transiting the region, with a focal length dependent on the difference in the electric field component along the direction of travel of the particles.

	Hex grid	45° line grid	90° line grid
$2\tilde{\theta}$	αR	$1.63\alpha R$	$2.31\alpha R$

Table C.1: Variation of the grid perturbation of the emittance with grid structure. The quantity α depends on the difference in longitudinal electric field on the two sides of the grid, and R is the radius of a circular aperture or the half-spacing of wires making up the grid.

A circular aperture under the same conditions gives a focal length

$$f_{\mathrm{C}} = \frac{4T}{\Delta E_{\parallel}} \qquad (C.5)$$

in each transverse plane. We have used both parallel-wire grids and metal honeycomb grids, which we will model as arrays of slit and circular apertures, respectively. The radial angular impulse $\Delta\theta_{\mathrm{r}}$ for a particle transiting a circular aperture is

$$\Delta\theta_{\mathrm{r}} = \alpha r$$

as a function of the distance r from the center of the aperture, so we may calculate $\langle\theta_{\mathrm{r}}^2\rangle$ as

$$\langle\theta_{\mathrm{r}}^2\rangle = \frac{2\pi \int_0^R (\alpha r)^2 r\, dr}{2\pi \int_0^R r\, dr} = \frac{(\alpha R)^2}{2}$$

Because the perturbations in the two transverse planes are equal, and because $\langle\theta_r^2\rangle = \langle\theta_x^2 + \theta_y^2\rangle = \langle\theta_x^2\rangle + \langle\theta_y^2\rangle$, we have

$$2\tilde{\theta}_x = \alpha R \qquad (C.6)$$

The results are summarized in the Table C.1.

C.2 Termination of the Accelerating Field of the Injector

In the the low-perveance configuration of the injector, we did not grade the aperture plates exactly as for a planar Pierce diode. The applied field was peaked at the center of the gun to provide some additional focusing, so the field at the exit grid was somewhat below the planar diode value $4V_{\text{gun}}/3L_{\text{gun}}$, which has the value 2.3 MV/m. We will use $\Delta E_{\parallel} = 2$ MV/m, so that $\alpha = 3.125$ for $V_{\text{gun}} = 160$ kV.

In this configuration, the beam charge density ρ at the grid was $90\mu C/\text{m}^3$. We will compare the relative effect from the segmented beam space-charge by calculating $\Delta\theta$ as a function of distance from the center of a slab, due to the self-field of the individual slab over a distance in z of twice the wire separation (the wire separation is $2R$).

$$\Delta\theta(r) = \frac{qE_{\perp}}{mv_z}\frac{4R}{v_z} = \frac{2\rho R}{\epsilon_0 V_{\text{gun}}}r,$$

so that

$$f = \frac{r}{\Delta\theta(r)} = \frac{2V_{\text{gun}}}{4R\frac{\rho}{\epsilon_0}}. \qquad (C.7)$$

For a grid spacing of 0.062 in, the quantity $4R\rho/\epsilon_0$ is about 30 kV/meter, negligible with respect to the accelerating gradient of 2 MV/meter.

We estimate the intrinsic gun emittance from measurements with a 9 mm beam radius and relativistic β_r of 0.0016, using

$$\epsilon_I^2 = \epsilon_T^2 - \epsilon_G^2$$

where ϵ_T is the net emittance after the grid and

$$\epsilon_G = R_{\text{Beam}}(2\tilde{\theta}_x)\beta\gamma$$

	Line grid	Hex grid
ϵ_T	$(1.15\text{--}1.25)\times10^{-7}\pi$	$(1.3\text{--}1.4)\times10^{-7}\pi$
ϵ_G	$0.58\times10^{-7}\pi$	$0.73\times10^{-7}\pi$
ϵ_I	$(0.99\text{--}1.11)\times10^{-7}\pi$	$(1.07\text{--}1.19)\times10^{-7}\pi$

Table C.2: Intrinsic emittance of gun before grid passage

Grid geometry	Normalized Emittance $(10^{-7}\pi$ meter radian)	
	measured	calculated ($\epsilon_I = 1.1$)
0.063 in wire	1.3	1.44
0.050 in ribbon	1.4	1.33
0.125 in hex	1.75	1.6
0.0625 in hex	1.3	1.25

Table C.3: Relative effect of various terminating grids vs. calculation

The results are shown in Table C.2.

We compare four different grid geometries for the 120 kV gun, one at a time. We used wires on 0.062 in centers, ribbon material on 0.050 in centers, and 0.125 in and 0.062 in hex material, with $\Delta E_\parallel = 2$ MV/m, $R_B = 12$ mm, and relativistic $\beta_r = 0.0014$. Table C.3 summarizes the results.

C.3 Effect of Multiple Biased Grids

Now we calculate the effect of our multiple emittance-spoiling grids, for which the effective spacing is 4 mm. We have

$$(2\tilde{\theta}_G)^2 = (R_1\alpha_1)^2 + (R_2\alpha_2)^2 + (R_3\alpha_3)^2$$

For grids of uniform 0.125 in cell size, with relativistic $\beta_r = 0.0016$ and $R_B = 9$ mm, we obtain for the normalized emittance

$$\epsilon_G = 0.37\sqrt{4 + V + \frac{3}{8}V^2} \times 10^{-7}\pi \text{ meter radian,} \qquad (C.8)$$

where V is the voltage applied to the central grid in kV. For the 120 kV configuration, we had $\beta_r = 0.0014$, and the cell size of the second grid was 0.062 in. Numerically, with $R_B = 12$ mm, the normalized emittance is

$$\epsilon_G = 0.56\sqrt{4 + V + \frac{3}{16}V^2} \times 10^{-7}\pi \text{ meter radian} \qquad (C.9)$$

The results are shown along with measurements in Fig. C.2. The agreement is very reasonable, although the grid spacing for the 120 kV configuration may be somewhat different from that for the 160 kV case.

Performance of the Emittance Control Grids as a Function of Applied Potential, Compared with Measurement
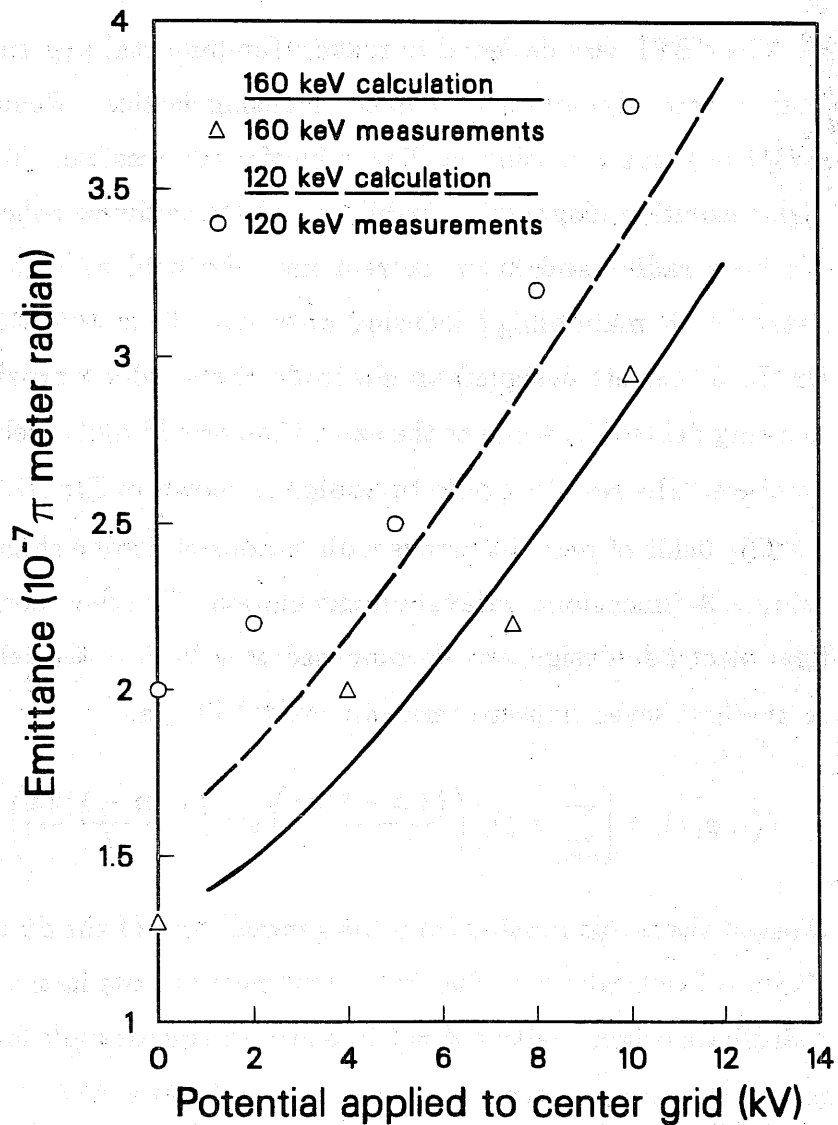
XCG 864-7170

Figure C.2: Grid spoiling of the emittance compared to calculated values.

Appendix D: Quadrupole Design

The SBTE was designed to make a fundamental experimental test of collective beam dynamics in a linear focusing lattice. Hence it is important that the actual focusing be linear insofar as possible. To enable detailed, high-resolution diagnostic capability, and to maximize collective effects, both the bore radius and beam current must be held as high as possible, consistent with maintaining focusing linearity. To satisfy these requirements, Dr. L. J. Laslett designed an electrode shape which provided highly linear focusing fields [50], while at the same time providing for relative ease of manufacture. The resulting pole-tip design is shown in Fig. D.1.

The fields of periodic arrays with various electrode shapes were examined using a 3-dimensional relaxation calculation. The field corresponding to the final electrode design was decomposed as a Fourier-Bessel series, truncated to the first seven nonzero terms in $\cos(2\theta)$ [50], as

$$V(r, \phi, z) = \left[\sum_{m=1}^{7} A_m I_2 \left(\frac{(2m-1)\pi r}{l} \right) \sin \left(\frac{(2m-1)\pi z}{l} \right) \right] \cos(2\phi). \quad (D.1)$$

Most of the terms missing from the general form of the Fourier-Bessel expansion are identically zero due to the symmetry of the lattice and the choice of coördinate origin. Setting $\phi = 0$ in one of the quadrupole focusing planes suppresses the $\sin(n\phi)$ terms; the potential is finite at $r = 0$, so the coefficients of the functions K_n are all zero; and choosing the z-origin so that $z = 0$ at the midplane between quadrupoles ensures that the $\cos \left(\dfrac{m\pi z}{l} \right)$ and $\sin \left(\dfrac{2m\pi z}{l} \right)$ coefficients are all zero. The values of n allowed by the lattice symmetry for the azimuthal dependence are of the form $4k + 2$, and we kept only the quadrupole, or $\cos(2\phi)$ terms for the field expansion used in later particle tracking and envelope integration programs. We list the coefficients for the
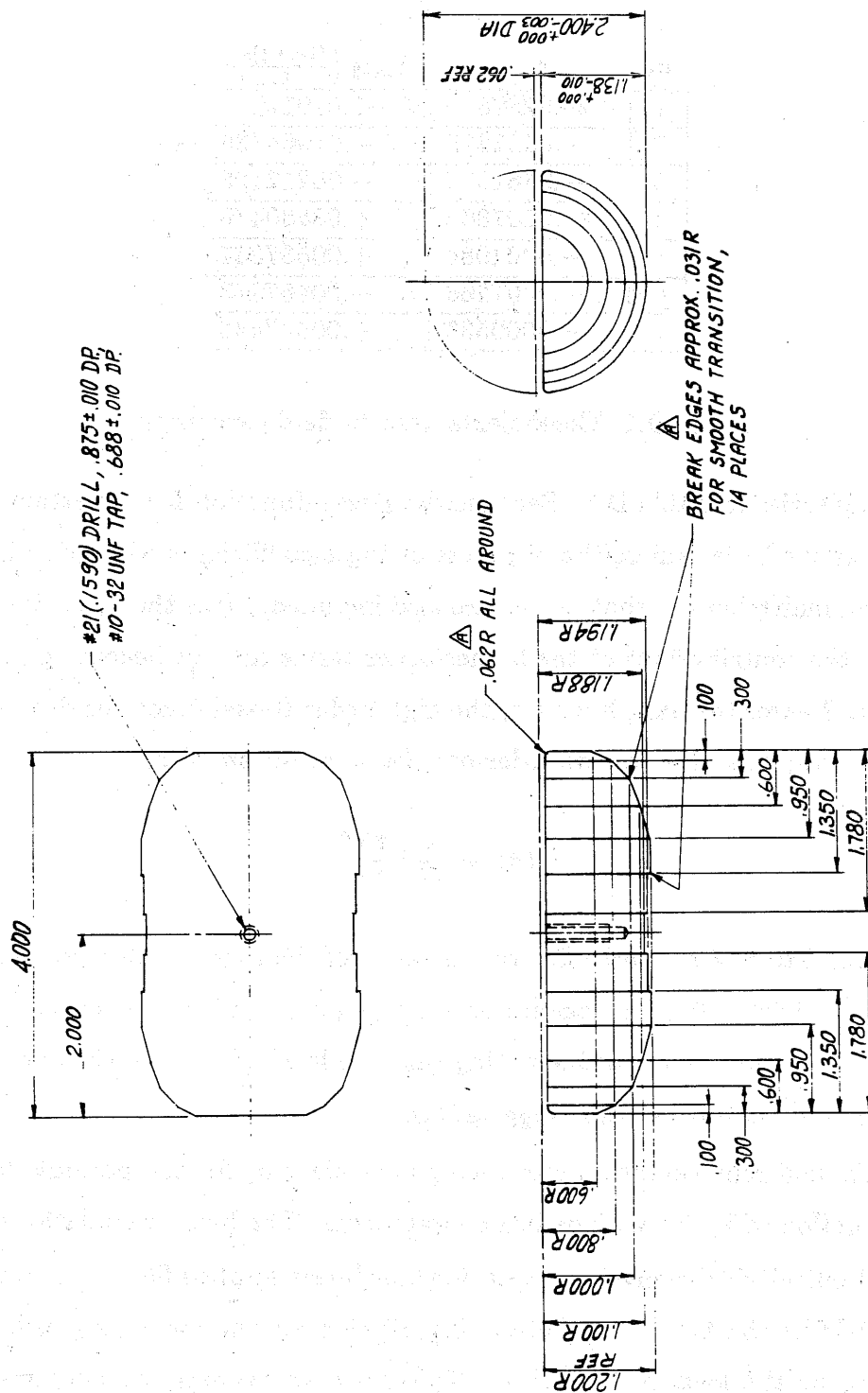
Figure D.1: SBTE electrostatic quadrupole dimensions.

XBL 865-1750

m	A_m	$A_m I_2 \left(\frac{(2m-1)\pi}{6} \right)$
1	+29.92578	+1.049172
2	−.0521235	−.01964735
3	−.0561377	−.08217125
4	+.0007866	+.03580476
5	+.0004084	+.00537351
6	−.0001266	−.00467973
7	+.0000533	+.00547446

Table D.1: Coefficients used in field expansion

resulting series in Table D.1. Because the Bessel function I_2 may attain large values at the bore radius, the products of these coefficients with their Bessel function multipliers at that radius are also included. Note that near the bore radius, the contributions of the higher-order terms are not becoming rapidly smaller. Nearer the axis, however, the high-order Bessel functions drop much more rapidly than the lowest-order one, because for small z,

$$I_n(z) \rightarrow \frac{1}{n!} \left(\frac{z}{2} \right)^n .$$

The peak value of the series for the listed coefficients for a 1.0 in radius and $\phi = 0$ is about 1.04, and occurs at a point on the electrode surface. The value here should be unity, indicating that the level of error in the expansion is about 4%, at least at this large radius.

This field representation was used to calculate σ_0 for the periodic lattice as a function of V_Q for various beam emittances. The beam calculations were carried out using the envelope equations for linear applied field by taking the local field at the beam edge, obtaining a value for the focusing gradient by dividing by the local beam radius. This gives an average focusing gradient over the beam diameter for use in the envelope equations, while including

the field nonlinearities in a very approximate way to take into account the variation in the focusing strength with beam radius. The value of σ_0 was obtained by performing the integral

$$\sigma_0 = \int_{z_0}^{z_0+2L} \frac{\epsilon \, dz}{R_x^2},$$

along with the beam envelope calculation, where the initial conditions had been chosen so that the beam was matched. As an additional check on the accuracy of the field representation, a comparison was made with the field generated from a relaxation calculation constrained to have $\cos(2\theta)$ symmetry. The resulting Fourier-Bessel coefficients were used in the same way to calculate the lattice σ_0 and the agreement between the two calculations for beam envelope values for $\sigma_0 \simeq 60°$ was better than 1 part in 10^5, giving support to the conclusion that Eqn. D.1 is an accurate description of the field within the periodic lattice of the SBTE.

Fig. D.2 shows $E_x(x)|_{y=0}$ for several values of z along a lattice period, and in Fig. D.3 we have plotted the values of σ_0 vs. a_{max} calculated for various input beam emittances with $I = 0$. The residual lattice nonlinearity is apparent in the variation of σ_0 with a_{max}.

For the lattice fields alone, it is relatively simple to determine the linearity of the focusing. However, in the high space-charge beam transport cases we wanted to investigate, the beam self-field provides a large perturbation to the lens fields, and is expected to be a strong source of field nonlinearity that could far outweigh the residual lens nonlinearity.

In summary, the lattice of the SBTE, using the electrode shape designed by Dr. Laslett, provides a good approximation to a linear focusing lattice, even with the extreme electrode length to bore radius ratio of 4 that was used. The short period length permitted a high average current density for
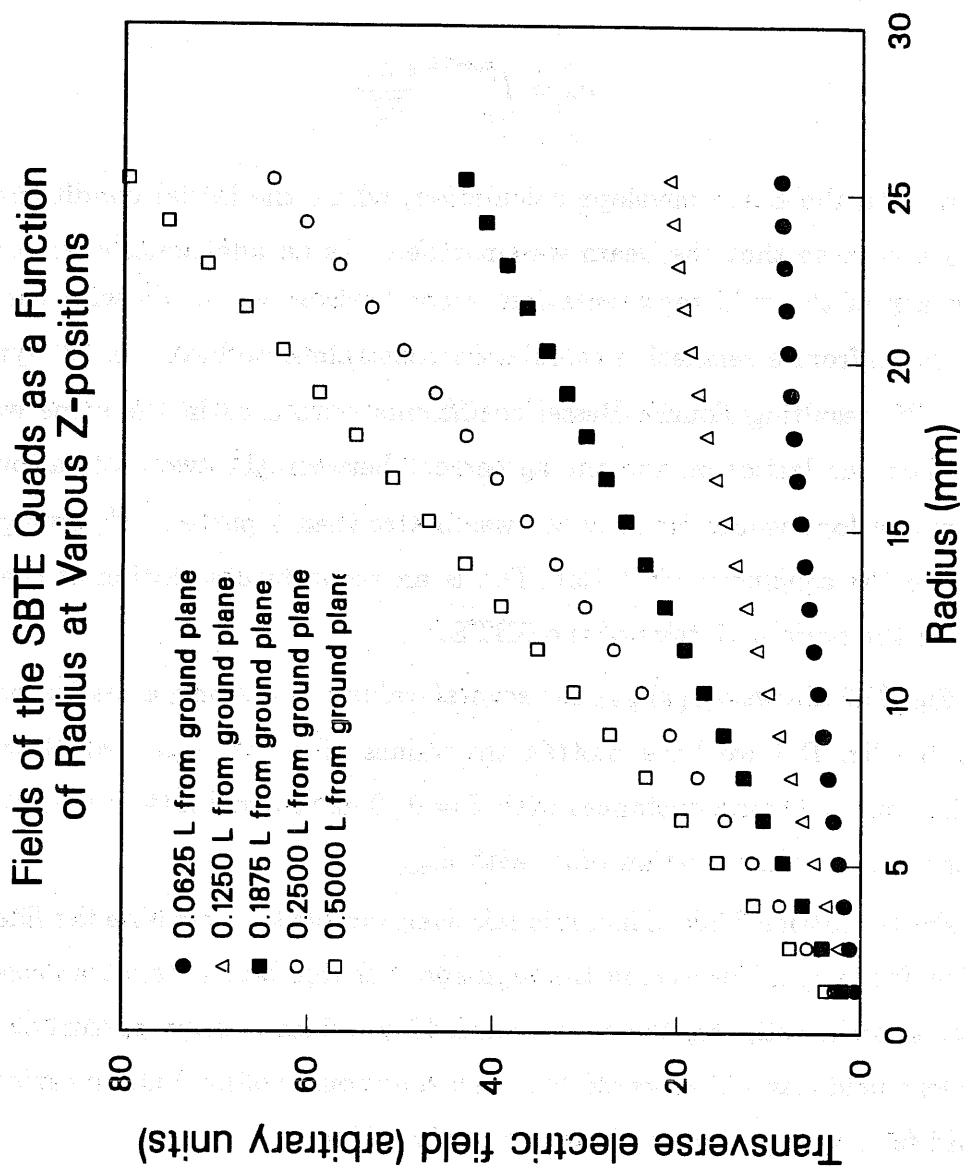
Figure D.2: Transverse field linearity of the SBTE periodic lattice.
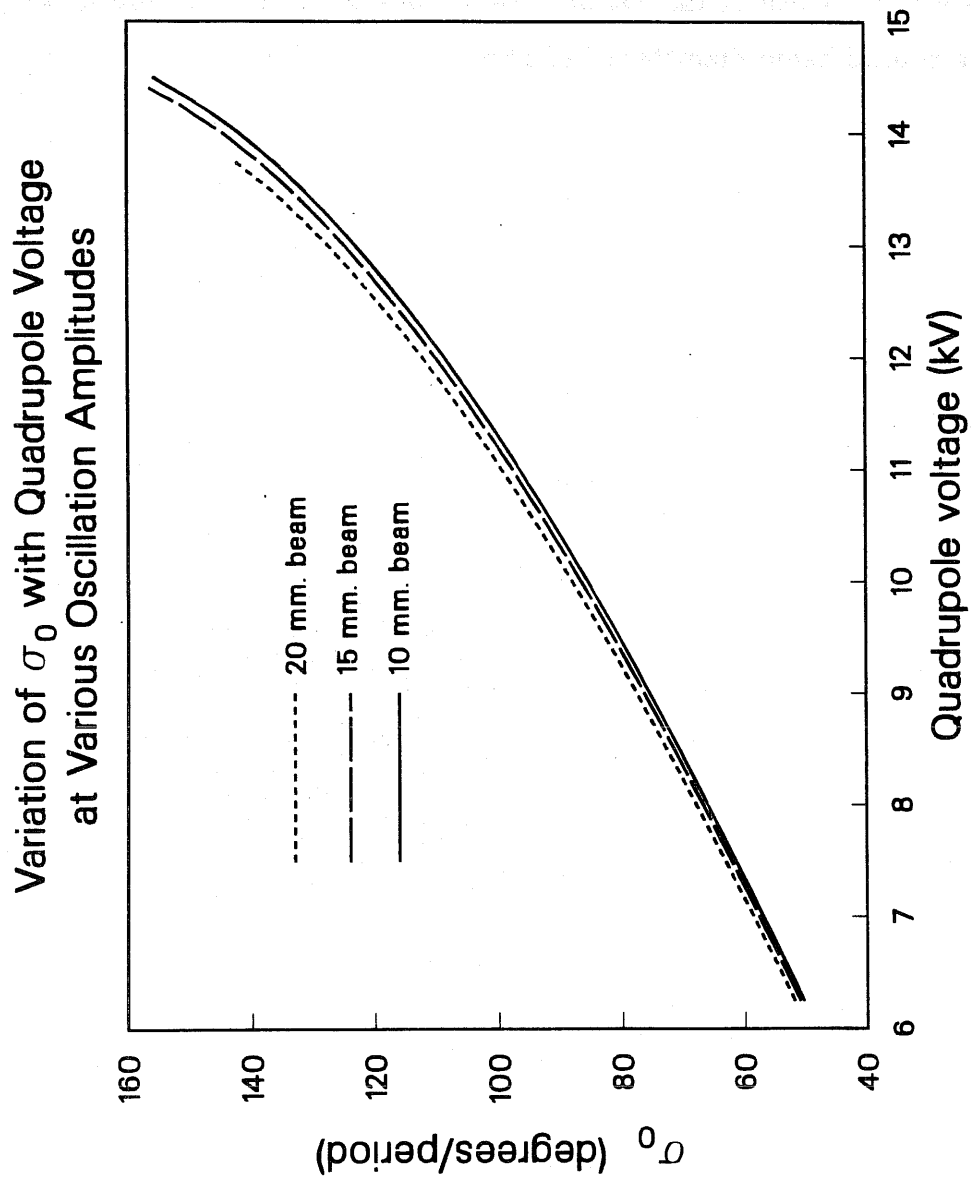
Figure D.3: Variation of σ_0 in the SBTE with particle oscillation amplitude.

space-charge dominated beam transport. Also, both the lens separation of 2 in and the large bore radius allowed high resolution diagnostics. For example, the sample width of the slit diagnostics was 0.010 in (0.25 mm), compared to a typical beam diameter of 12 mm.

Appendix E: Ion Sources

We discuss the features of the aluminosilicate sources used in SBTE, focusing primarily on the emitter surface coating quality and manufacturing techniques. We initially chose to purchase commercially available sources for our Cs^+ beam. We then found that in order to obtain the desired current, we must operate the sources at very close to the maximum heater power they could tolerate. As a result we burned out two heater filaments. In addition, the commercial coating of Cs-doped aluminosilicate material was insufficient for our use, because after 2–6 weeks in service (varying from source to source) the Cs^+ current became seriously diminished.

E.1 Source Recoating Procedure

The source bodies were satisfactory, although they would just barely maintain the temperature required to emit the desired current. After replacing several sources because of cesium depletion, we decided to recoat the emitter surfaces ourselves with an aluminosilicate mixture. Dr. S. S. Rosenblum mixed alumina, silica, and Cs_2CO_3 in the proper stoichiometric proportions for the β-eucryptite zeolite, and fused the material in an inert gas furnace. After he had re-pulverized the mixture, we applied it to the source bodies and found techniques described in the following for obtaining suitable adhesion between the aluminosilicate and the substrate.

We constructed a vacuum furnace of simple design (a cylindrical winding of 0.03-inch tantalum wire large enough to encircle the source—about 2 inches in diameter—and about 4 inches tall, supported by high-grade alumina tubing with slots cut for support of the hot wire, and surrounded by about 10 layers of 0.002-inch molybdenum foil to serve as a heat shield, all mountable in a small vacuum chamber that was available) and baked the spent sources at 1700°C for 10 minutes. The overall cycle time was about 30 minutes to

1700°C, 10 minutes at 1700°C, and then power off. We applied the powdered aluminosilicate (200 mesh) to the emitter surface in slurry form, using either distilled water or methanol, to a depth of about 0.010–0.020 inch. After pumping the liquid away in the vacuum for several hours, we raised the temperature as rapidly as possible, consistent with keeping the pressure reading below 10^{-4} Torr. A substantial amount of vapor was evolved, possibly CO_2 entrained in the aluminosilicate in addition to the remaining carrier fluid for the coating. The furnace cycle was similar to the bake cycle for cleaning the sources.

The stack of heat shields at the top of the furnace had a hole through it, permitting optical measurements of the temperature. The pyrometer filters and optics permitted me to observe when the aluminosilicate mixture began to fuse. After the coating began to fuse visibly, we quenched the furnace by venting it with argon gas and turning off the heater power. The argon quench was an attempt to collapse small bubbles (of CO_2?) of 0.01–0.02-inch diameter in the molten aluminosilicate before the material solidified.

The new coatings were sometimes too thick, and the thermal conductivity was apprarently too low to allow the emitter surface to reach the required temperature. The pyrometer-measured temperature of the emitter surface was below the temperature of the commercially coated sources by about 50°C. After we ground the coating down to a thickness of about 0.010 inch, the temperature returned to its former value and the Cs^+ current rose to useful levels. The bubbles mentioned above were visible in the surface of the aluminosilicate, and can cause inhomogeneous emission of the ion beam. Transverse fields near the surface capable of degrading the emittance by a large factor over the intrinsic thermal emittance can easily result. The test stand geometry was not the same as the SBTE gun, so final tests had to be done in the actual SBTE gun.

E.2 Performance

E.2.1 Current

The new coatings provided marginally higher beam current than the original sources. However, the major gain was in longevity. The first of the two recoated sources we used lasted for nine months of regular use, and the second lasted for over a year. The source presently in use is a test formulation made by A.A. Warwick during his research on source fabrication for the MBE-4 accelerator experiment [51].

E.2.2 Source Emittance

The lower bound ϵ_{min} on the normalized source emittance ($4\epsilon_{RMS}$) is given by the source radius, R_S, and the mean thermal energy $\dfrac{kT}{2}$ in each transverse plane as

$$\epsilon_{min} = 2R_S\sqrt{\frac{kT}{mc^2}} = 0.23 \times 10^{-7}\pi \text{ meter radian.} \qquad (E.1)$$

This is about a factor of 5 below the measured beam emittance, and indicates that there is a significant perturbation to the transverse velocity spread of the particles even before they exit the gun. Additional perturbations to the emittance of the beam, due to passage through grids at the exit of the gun, are calculated and compared with measurements in Appendix C.

E.2.3 Beam Purity

When our in-house sources were first installed, the Cs^+ beam was very pure. As the sources aged, they all began to yield a small proportion of light ions along with the bulk Cs^+ beam. The appearance of the light ions is accompanied by a decrease in the cesium component of the beam. When the light-ion fraction grew to about 5%, the source was no longer deemed

satisfactory, and it was replaced at that time.

The light ions separate themselves from each other and from the cesium component by time-of-flight in short-pulse beam operation. This effect was used to analyze the mass spectrum of the light ions. We did this after the useful life of the first recoated source we used, during the initial operation of the injector in its shortened configuration. With more current being drawn from the injector, the light ion fraction had risen to nearly 20%. We took this opportunity to measure the relative proportion of various mass numbers in the beam, rather than replace the source immediately.

Near the source, before the light ions separate from the bulk cesium beam, they experience the fields of the cesium component. Because static electric fields function as energy separators, rather than momentum separators as do magnetic fields, the light ions respond exactly as do the cesium ions to the self- and external fields. Later in the lattice, when they leave the bulk Cs^+ beam and its space-charge fields, they are mismatched, and a large proportion is lost to the walls. About one-third of the light ion component was lost after separating from the bulk Cs^+ beam, based on Faraday cup measurements along the lattice.

As the light ion components separated in time, downward steps in the trailing edge of the current pulse, measured at the end of the transport line, allowed the masses to be calculated from time-of-flight. This is similar the trailing step visible on the current pulses in Fig. 5.3. By far the largest light-ion component was at $A = 28$ (calculated with respect to the ^{133}Cs time of flight). Masses of other trace components were calculated with respect to the $A = 28$ component. This main component ($A = 28$) accounted for almost 90% of the total light ions. Both silicon ($A = 28$) and aluminum ($A = 27$) are components of the emitter, and metallic aluminum is the material forming

A	I (mA)	% of light ions	Possible species (based on A/q)
16	0.03	1.5	O^+ (16)
28	1.7	88.	Si^+ (28), Al^+ (27)
31	0.08	4.	O_2^+ (32)
39	0.05	3.	K^+ (40)
44	0.04	2.	SiO^+ (44), AlO^+ (43)
48–49	0.01	0.5	$Al_2O_3^{+2}$ (51)
57	0.01	0.5	AlO_2^+ (57), SiO_2^+ (58)
74	0.01	0.5	Al_2O^+ (70), AlO_3^+ (75)
86	0.01	0.5	$Al_2O_2^+$ (86)

Table E.1: Distribution of light ion impurities

most of the gun structure, and both are probably present in this mass peak. Other ion masses obtained assuming the mass of the major component to be 28 were consistent with a number of dissociation products of Al_2O_3 and SiO_2. The mass determination could be in error by ± 2 amu. Results are shown in Table E.1. We also note that there was a time delay of about 200–300 ns after the Cs^+ emission began before the light ion emission began. By applying very short pulses to the gun, we were able to obtain Cs^+ currents of more than 75% of the steady-state level with no measurable light ion component.